
Numerical Heat Transfer, Part A: Applications: An International Journal of Computation and Methodology

Publication details, including instructions for authors and subscription information:
http://www.tandfonline.com/loi/unht20

# Three-Dimensional Numerical Study of Fluid and Heat Transfer Characteristics of Dimpled Fin Surfaces

J. F. Fan [a], W. K. Ding [a], Y. L. He [a] & W. Q. Tao [a]

[a] Key Laboratory of Thermo-Fluid Science and Engineering of MOE, School of Energy & Power Engineering, Xi'an Jiaotong University, Xi'an, Shaanxi, P.R. China

Version of record first published: 02 Aug 2012.

To cite this article: J. F. Fan , W. K. Ding , Y. L. He & W. Q. Tao (2012): Three-Dimensional Numerical Study of Fluid and Heat Transfer Characteristics of Dimpled Fin Surfaces, Numerical Heat Transfer, Part A: Applications: An International Journal of Computation and Methodology, 62:4, 271-294

To link to this article: http://dx.doi.org/10.1080/10407782.2012.666931

*Numerical Heat Transfer, Part A*, 62: 271–294, 2012

ISSN: 1040-7782 print/1521-0634 online
DOI: 10.1080/10407782.2012.666931

Taylor & Francis
Taylor & Francis Group



# THREE-DIMENSIONAL NUMERICAL STUDY OF FLUID AND HEAT TRANSFER CHARACTERISTICS OF DIMPLED FIN SURFACES

**J. F. Fan, W. K. Ding, Y. L. He, and W. Q. Tao**
*Key Laboratory of Thermo-Fluid Science and Engineering of MOE, School of Energy & Power Engineering, Xi'an Jiaotong University, Xi'an, Shaanxi, P.R. China*

***In the present study, a code based on the nonorthogonal curvilinear coordinates is developed with a collocated grid system generated by the two-boundary method. After validation of the code, it is used to compare simulated results for a fin-and-tube surface with coupled and decoupled solution methods. The results of the coupled method are more agreeable with the test data. Simulation for dimpled and reference plain plate fin-and-tube surfaces are then conducted by the coupled method within a range of inlet velocity from 1.0 m/s to 5 m/s. Results show that at identical pumping power the dimpled fin can enhance heat transfer by 13.8–30.3%. The results show that relative to the reference plain plate fin-and-tube surface, heat transfer rates and pressure drops of the dimpled fin increase by 13.8%–30.3% and 31.6%–56.5% for identical flow rate constraint. For identical pumping power constraint and identical pressure drop constraint, the heat transfer rates increase by 11.0%–25.3% and 9.2%–22.0%, respectively. By analyzing the predicted flow and temperature fields it is found that the dimples in the fin surface can improve the synergy between velocity and fluid temperature gradient.***

## 1. INTRODUCTION

Studies on enhancing heat transfer have been conducted along the lines of understanding enhancement mechanisms and developing enhancing techniques. The recently developed field synergy principle [1–4] is one of the successful research results in the study of the mechanism. According to this principle the better the synergy between velocity and temperature gradient, the more intensive the heat transfer is between solid and fluid. It is found by the field synergy principle [3, 5–7] that the fin surface can not only increase the heat transfer area but also greatly improve the synergy between the velocity and temperature gradient. Before the development of the field synergy principle, different kinds of plate fin-and-tube surfaces had been developed and adopted as important enhancing structures, including wavy fin,

Received 1 April 2011; accepted 3 February 2012.
The present work is supported by National Fundamental Research R&D of China (G 2011CB710702) and the Key Project of NNSFC(51136004).
Address correspondence to W. Q. Tao, Key Laboratory of Thermo-Fluid Science and Engineering of MOE, School of Energy & Power Engineering, Xi'an Jiaotong University, Xi'an, Shaanxi, P.R. China. E-mail: wqtao@mail.xjtu.edu.cn

## NOMENCLATURE

| | |
|---|---|
| $\alpha$ | coefficient of discrete equation |
| $A_o$ | total heat transfer surface area, $m^2$ |
| $b$ | source term of discrete equations |
| $c_p$ | heat capacity, $kJ \cdot kg^{-1} \cdot K^{-1}$ |
| $dA$ | heat transfer surface area, $m^2$ |
| $d_o$ | characteristic size, m |
| $D_0$ | tube outside diameter, m |
| $e_i$ | basic vector in oblique curvilinear coordinates |
| $e^i$ | reciprocal basic vectors in oblique curvilinear coordinates |
| $\sqrt{g}$ | Jacobi factor, $e_i \cdot (e_j \times e_k)$ |
| $g^{ij}$ | metric tensor, $e^i \cdot e^j$ |
| $h_o$ | convection heat transfer coefficient, $W \cdot m^{-2} \cdot K^{-1}$ |
| $HQD$ | dimple height, m |
| $J$ | total flux density of convection and diffusion, $Wm^{-2}$ |
| $l$ | air flow channel length, m |
| $p$ | pressure, Pa |
| $p'$ | pressure-correction value, Pa |
| $P$ | pumping power, W |
| $q_m$ | mass flow, $kg \cdot s^{-1}$ |
| $Q$ | heat transfer rate, W |
| $R$ | source term in oblique curvilinear coordinates |
| $RA, RB, RC$ | three axes length of ellipsoid, m |
| $RQ_b$ | radius of circular in stamped surface, m |
| $RQA, RQB$ | major and minor axes of ellipse in stamped surface, m |
| $S$ | source term in the Cartesian coordinate system |
| $S_1$ | transverse tube spacing, m |
| $S_2$ | longitudinal tube spacing, m |
| $T_{in}$ | inlet temperature of air, K |
| $T_{out}$ | outlet temperature of air, K |
| $T_w$ | wall temperature of tube, K |
| $T$ | temperature, K |
| $u$ | velocity in the Cartesian coordinate system, $m \cdot s^{-1}$ |
| $u_m$ | mean flow velocity in the minimum free area, $m \cdot s^{-1}$ |
| $U, V, W$ | contravariant velocity components in curvilinear coordinates, $m \cdot s^{-1}$ |
| $V$ | volume, $m^3$ |
| $\vec{V}$ | velocity vector in curvilinear coordinates, $m \cdot s^{-1}$ |
| $V^i$ | contravariant velocity in curvilinear coordinates, $m \cdot s^{-1}$ |
| $x$ | coordinate component in the Cartesian coordinate system, m |
| $\Gamma_\phi$ | generalized diffusion coefficient, $Pa \cdot s$ |
| $\Gamma^j_{ik}$ | second remark of Christoffel, $e^i \cdot \partial e_j / \partial \xi^k$ |
| $\Delta p$ | pressure drop, Pa |
| $\nabla T$ | temperature gradient, K |
| $\phi$ | solving variable |
| $\Phi$ | total heat transfer rate from the hot to the cold fluid, W |
| $\delta$ | fin thickness, m |
| $\zeta, \eta, \xi$ | coordinates component in curvilinear coordinates, m |
| $\xi^k$ | coordinates component in curvilinear coordinates, m |
| $\theta_m$ | mean synergy angle |
| $\lambda_a$ | thermal conductivity of air, $W \cdot m^{-1} \cdot K^{-1}$ |
| $\mu$ | dynamic viscosity, $kg \cdot m^{-1} \cdot s^{-1}$ |
| $\nu_a$ | kinematic viscosity of air, $m^2 \cdot s^{-1}$ |
| $\rho$ | density, $kg \cdot m^{-3}$ |

**Superscripts**

| | |
|---|---|
| $i, j$ | summation indicators |
| $k$ | free indicator |
| $e, w, n, s, t, b$ | faces of control volume of main node |
| $\zeta, \eta, \xi$ | component in curvilinear coordinates |

**Subscripts**

| | |
|---|---|
| $a$ | air |
| $d$ | dimpled fin |
| $e, w, n, s, t, b$ | faces of control volume of main node |
| $E, W, N, S, T, B$ | node adjacent to the main node |
| $i, j$ | summation indicators |
| $k$ | free indicator |
| $m$ | mean |
| $P$ | main node |
| 0 | plain plate fin |
| 1, 2, 3 | coordinates component in curvilinear coordinates |

louvered fin, slotted fin, and fin with longitudinal vortices generators. Application of the field synergy principle further improves the structure of the slotted fin-and-tube surfaces [5, 6].

In the study of heat transfer enhancement, both experimental [8–13] and numerical methods have been used, and with the rapid development of computer technology the numerical method becomes more and more popular and reliable. Numerical methods can obtain detailed results of temperature and velocity field, which are very useful to the analysis for further improvement of the geometric structure studied. In this study, numerical method will be used to predict the performance of a new-type enhanced surface.

As far as the numerical approach is concerned, since the flows in the plate fin-and tube heat exchangers are incompressible the pressure-correction method, representative by the SIMPLE algorithm, based on a staggered grid arrangement has been predominantly adopted [5–7, 14, 15] to deal with the coupling between pressure and velocity. A staggered grid system can successfully overcome the difficulty of checker board pressure distribution [16, 17], and hence, have been widely adopted in computational fluid dynamics and heat transfer. However, its implementation is somewhat more complicated than the nonstaggered grid system. With the increasing of domain complexity this drawback becomes more obvious. In 1983, Rhie and Chow [18] proposed the idea of a nonstaggered grid and momentum interpolation method for interface velocity to deal with the appropriate coupling between velocity and pressure, and in 1988 Peric et al. [19] further expounded this issue; henceforth, the collocated grid has been developed rapidly [20–22]. The advantages of the collocated grid are especially prominent for the domains in nonorthogonal curve coordinates which will be used in the present numerical study.

In the simulation of heat transfer characteristics of a fin-and-tube structure careful attention should be paid to the boundary condition of the fin surface. Actually, the heat conduction in the fin and convection heat transfer over the fin surface are mutually coupled with each other. This is the so-called conjugated problem in the computational heat transfer [16, 17]. In this kind of problem the boundary conditions of the fluid-solid interface is not known a priori but is the result of the calculation. Since 1978 when Patanker conducted the numerical simulation of conjugated heat transfer for a thick-walled rectangular channel with uniform outer surface temperature [23], much numerical research has been made [5, 14, 24–28]. But these studies were mainly based on the staggered grid arrangement in Cartesian coordinates, and the stepwise approximation was usually used for simulating the curve boundary in irregular region. For a complicated fin-tube structure, the nonorthogonal curvilinear coordinates system have obvious advantages in approximating irregular boundaries.

Now, attention is turned to the air-side enhanced techniques. Apart from the plate fin-and-tube surfaces mentioned above and vortex generators [29–31], a new type of attractive enhanced heat transfer surface, called the dimple surface, have been extensively studied in the literature [32–44]. Originally, dimples were used in internal cooling passages [33–36]. In this article, they are used to enhance heat transfer of a plain plate fin-and–tube surface and their performance will be numerically investigated.

Dimples are arrays of indentations along surfaces. Generally, these are spherical in shape, while a variety of other shapes have also been employed, ranging from

triangular to tear drop. The influences of different arrangements and geometric parameters on flow and heat transfer characteristics have been investigated by experimental method in cooling passages, and the flow visualization investigations reveal that the flow structure in the dimple is mainly of vortex type. Because the dimples do not protrude into the flow to produce significant amounts of form drag, the dimpled surface generally produces lower friction penalties compared with several other types of augmentation ones. When dimples are used in the fin-and-tube surface, on one side of the fin there are indentations, and on the other side there are protrusions or turbulators. The vortices generated can enhance the local and downstream heat transfer.

In this article, a computational code for simulating a conjugated heat transfer problem of a complicated fin-and-tube surface with dimpled structures will be developed by a nonorthogonal curvilinear coordinates system with collocated grid arrangement. After validation of the code it is then used to simulate the heat transfer and fluid flow characteristics of the new type fin surfaces, i.e., dimpled fin surfaces. In the proposed dimpled fin surface an array of staggered shallow ellipsoid dimples are stamped along the fin surface. The present numerical investigation is focused on engineering applications in lower velocities; hence, laminar flow is assumed. In addition, the fluid thermophysical properties are regarded as constant.



## 2. SIMULATION OF FLUID-SOLID COUPLING HEAT TRANSFER WITH COLLOCATED CURVILINEAR NONORTHOGONAL GRIDS

The effective numerical methods for solving a conjugated problem can be classified into two types: domain decomposition with interface information exchanges and solving the whole-field with general governing equations (hereafter, it will be simply called whole-field solving) [15]. The former is that the fluid and solid areas are solved separately; thus, for the momentum equation only the fluid region needs to be solved. In this regard, some saving may be made in the computing time, however, the interface information exchange may take some additional computational time. For the following reasons the whole-field solving method will be used here. First, in the computational domain of a fin-and-tube unit the two directions in the streamwise flow direction and in the spanwise direction are often much larger than the direction of fin pitch. Such geometric structure may lead to some difficulty in solution convergence, and the shorter the fin-pitch direction the severer the difficulty. If the whole-field solving method is used, the height of this direction is obviously larger than that of the two regions in the domain decomposition method. According to the authors' practice, this will help to accelerate the convergence process. Second, when the entire field is taken as computational domain, the mass and flux continuity conditions at the solid-fluid interface will be automatically satisfied. When the harmonic-mean method (with special care to be mentioned later) is adopted to deal with large difference in thermophysical properties between solid and fluid, the entire field containing both solid and fluid can be solved with ease.

In the following, the general governing equations and boundary conditions will first be presented, followed by a detailed description of a grid generation method to deal with the irregular geometry. The details of numerical treatment for the conjugated problem in a collocated grid system with nonorthogonal curvilinear

coordinates will be presented. Then, numerical results of fluid flow and heat transfer surfaces for the dimpled fin-and-tube surfaces will be provided, and discussion from the view point of the field synergy principle will be presented. Finally, some conclusions will be drawn.

### 2.1. Transformation of Governing Equations

In the three-dimensional coordinates the general governing equations for steady, incompressible, laminar flow with constant physical properties can be expressed by the following vector form of scalar variables:

$$\nabla \cdot (\rho \vec{V} \phi) = \nabla \cdot (\Gamma_\phi \nabla \phi) + S_\phi \tag{1}$$

where $\phi$ is the general scalar variable, and when $\phi = 1$, $u_k$, $T$, Eq. (1) represents the continuity equation, momentum equation and the energy equation, respectively; $\Gamma_\phi$ is the generalized diffusion coefficient, and $>\Gamma_\phi = 0$, $\mu$, $\lambda/c_p$ represent the diffusion coefficient of the above three equations, respectively; and $S_\phi$ is the generalized source term, and $S_\phi = 0$, $-\partial p/\partial x_k$, 0 represent the source term of the above three equations, respectively.

In order to cope with the irregular shape of the dimple, we need to transform the governing equations from an orthogonal coordinate system to a curvilinear nonorthogonal coordinate system by tensor calculus. In the nonorthogonal coordinates there are a number of choices for the dependent variables. However, from the satisfaction of conservation law, it is found that the choice of physical velocity components of the Cartesian coordinates for the momentum equations in conjunction with the contravariant component of velocity at the interface for the continuum equation is the best one [45]. In this article, this practice is adopted. The details of the transformation are omitted here. Following is the transformed results of the general governing equation:

$$\frac{\partial(\sqrt{g}\rho\phi V^i)}{\partial \xi^i} = \frac{\partial}{\partial \xi^i}\left(\Gamma_\phi g^{ji} \frac{\partial \phi}{\partial \xi^j}\sqrt{g}\right) + \sqrt{g} R_\phi \tag{2}$$

where $R_\phi$ is a general source term of the governing equations in the curvilinear coordinates, and $R_\phi = 0$, 0, $-A_k^i(\partial p/\partial \xi^i)$ for the continuity, energy and momentum equations in the computation domain, respectively.

The diffusion term can be decomposed into an orthogonal ($i = j$) and a nonorthogonal ($i \neq j$) part. In order to ensure that the coefficient matrix of discretized equations is unconditionally diagonally dominant, the nonorthogonal terms is incorporated into the source term and is treated explicitly. So, the transformed general form of the governing equations is as follows.

$$\frac{\partial(\sqrt{g}\rho\phi V^i)}{\partial \xi^i} = \frac{\partial}{\partial \xi^i}\left(\Gamma_\phi g^{ii} \frac{\partial \phi}{\partial \xi^i}\sqrt{g}\right) + \left[\sqrt{g} R_\phi + \frac{\partial}{\partial \xi^i}\underset{i\neq j}{\left(\Gamma_\phi g^{ji} \frac{\partial \phi}{\partial \xi^j}\sqrt{g}\right)}\right] \tag{3}$$

where the last term in the square bracket of the right-hand side of Eq. (3) is the extended source term of the general governing equation, into which the nonorthogonal diffusion terms are included.

The general variable in the above equation is a scalar one which stands for the temperature and velocity components. Based on the finite-volume concept, a general discretized equation for the momentum and energy equations can be obtained as follows.

$$a_P\phi_P = a_E\phi_E + a_W\phi_W + a_N\phi_N + a_S\phi_S + a_T\phi_T + a_B\phi_B + b \tag{4}$$

where $a_k$ and $b$ are coefficient and source term of the discretized equation, respectively.

It is worth noting that the coefficient $a_k$ includes the influence of convection and diffusion actions, and it depends on $F$ and $D$, i.e., $a_k = f_k(F, D)$, where $F$ is the flow rate at the control volume interface and $D$ is the interface diffusion conductivity. The specific form of the function $f_k$ depends on the discretization scheme and can be found in reference [17]. In the nonorthogonal curvilinear coordinates $F$ and $D$ can be determined as follows

$$\begin{aligned}
F_e &= (\rho\sqrt{g}V^{\xi}\Delta\eta\Delta\zeta)_e,\ D_e = \left(\frac{\Gamma_\phi\sqrt{g}g^{\xi\xi}}{\delta\xi}\Delta\eta\Delta\zeta\right)_e;\ F_w = (\rho\sqrt{g}V^{\xi}\Delta\eta\Delta\zeta)_w \\
D_w &= \left(\frac{\Gamma_\phi\sqrt{g}g^{\xi\xi}}{\delta\xi}\Delta\eta\Delta\zeta\right)_w; F_n = (\rho\sqrt{g}V^{\eta}\Delta\xi\Delta\zeta)_n, D_{\mathrm{n}} = \left(\frac{\Gamma_\phi\sqrt{g}g^{\eta\eta}}{\delta\eta}\Delta\xi\Delta\zeta\right)_{\mathrm{n}} \\
F_s &= (\rho\sqrt{g}V^{\eta}\Delta\xi\Delta\zeta)_s,\ D_s = \left(\frac{\Gamma_\phi\sqrt{g}g^{\eta\eta}}{\delta\eta}\Delta\xi\Delta\zeta\right)_s; F_t = (\rho\sqrt{g}V^{\zeta}\Delta\xi\Delta\eta)_t \\
D_t &= \left(\frac{\Gamma_\phi\sqrt{g}g^{\zeta\zeta}}{\delta\zeta}\Delta\xi\Delta\eta\right)_t; F_b = (\rho\sqrt{g}V^{\zeta}\Delta\xi\Delta\eta)_b,\ D_b = \left(\frac{\Gamma_\phi\sqrt{g}g^{\zeta\zeta}}{\delta\zeta}\Delta\xi\Delta\eta\right)_b \\
b &= \sqrt{g}R_\phi\Delta\xi\Delta\eta\Delta\zeta + (\Gamma_\phi\sqrt{g}g^{\xi\eta}\phi_\eta\Delta\eta\Delta\zeta)_w^e + (\Gamma_\phi\sqrt{g}g^{\xi\zeta}\phi_\zeta\Delta\eta\Delta\zeta)_w^e \\
&\quad + (\Gamma_\phi\sqrt{g}g^{\xi\eta}\phi_\xi\Delta\xi\Delta\zeta)_s^n + (\Gamma_\phi\sqrt{g}g^{\xi\eta}\phi_\xi\Delta\xi\Delta\zeta)_s^n \\
&\quad + (\Gamma_\phi\sqrt{g}g^{\eta\zeta}\phi_\zeta\Delta\xi\Delta\zeta)_s^n + (\Gamma_\phi\sqrt{g}g^{\xi\zeta}\phi_\xi\Delta\xi\Delta\eta)_b^t + (\Gamma_\phi\sqrt{g}g^{\eta\zeta}\phi_\eta\Delta\xi\Delta\eta)_b^t
\end{aligned} \tag{5}$$

To deal with the coupling between pressure and velocity, the SIMPLE algorithm will be adopted. For the pressure correction, the following discretized equation can be obtained.

$$a_P p' = \sum_{nb} a_{nb}p'_{nb} + b \tag{6}$$

where

$$\begin{aligned}
a_E &= (\rho\Delta_1)_e;\ a_W = (\rho\Delta_1)_w;\ a_N = (\rho\Delta_2)_n;\ a_S = (\rho\Delta_2)_s;\ a_B = (\rho\Delta_3)_b \\
a_T &= (\rho\Delta_3)_t;\ \Delta_k = (A_j^k)^2/a_P^{(u_j)};\ a_P = a_E + a_W + a_N + a_S + a_T + a_B \\
b &= (\rho U^*)_w - (\rho U^*)_e + (\rho V^*)_s - (\rho V^*)_n + (\rho W^*)_b - (\rho W^*)_t
\end{aligned} \tag{7}$$

The contravariant velocities at the control volume faces are needed when the convective mass flux at the control volume faces is to be estimated. In order to overcome the checkerboard oscillations in pressure, a close coupling between pressure and velocity is required. This is achieved by the Rhie and Chow interpolation method in the collocated grid system [18].

### 2.2. Numerical Techniques for the Conjugated Problem in Collocated Grid System

In numerical simulation of fluid flow and heat transfer problems within irregular geometries, especially for three-dimensional irregular domain, the collocated grid system in the nonorthogonal coordinates have their special advantages. For the fluid-solid coupling problem in the staggered gird system, the numerical treatment techniques have been well-developed [17]. However, for the collocated grid system some special care should be taken. It is well-known that the influencing factor $a_{nb}$ in Eq. (4) represents the influence of convection and diffusion of the adjoining node on the main node $P$ through the interface. For different discretization schemes, the factor $a_{nb}$ is always the function of Peclect number $P_\Delta(P_\Delta = F/D)$ at the interface. So the variables $F$ and $D$ at the interfaces of control volume needed to be calculated first in order to obtain the value of factor. Taking the solid-fluid interface shown in Figure 1 as an example, the numerical details for the determination of $F$ and $D$ and other related issues are presented as follows.

**2.2.1. Calculation of flow rate through a solid-fluid interface which coincides with a control volume interface.** As shown in Figure 1, $W$ is the west node adjacent to the main node $P$; $w$ represents both the fluid-solid coupling interface and interface of control volume $P$. The region from west node $W$ to interface $w$ is fluid area, and from $w$ to the main node $P$ is a solid one. At the interface $w$, both the values of the normal velocity and the flow rate $F$ should always be zero. This is guaranteed in the simulation by always taking the interface velocity to be equal to 0.

**2.2.2. Calculation of diffusion conductance through a solid-fluid interface which coincides with a control volume interface.** The diffusion flux through the interface w can be expressed by tensor form as follows.

$$J_w = (\Gamma \nabla \phi \cdot dA)_w \tag{8}$$

By tensor notation, the diffusion flux can be written [46] as follows.

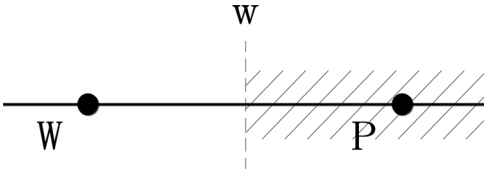


**Figure 1.** Schematic diagram of fluid-solid coupling calculation.

$$J_w = \left(\Gamma \varepsilon_{\eta\zeta\xi} g^{\xi\xi} J d\eta d\zeta \frac{\partial \phi}{\partial \xi}\right)_w = (g^{\xi\xi} J d\eta d\zeta)_w \left(\Gamma \frac{\partial \phi}{\partial \xi}\right)_w \tag{9}$$

The discretization expression of the diffusion flux is

$$J_w = (\Gamma g^{\xi\xi} J \Delta\eta\Delta\zeta)_w \frac{\phi_W - \phi_P}{(\Delta\xi)_w} = D_w \frac{\phi_W - \phi_P}{(\Delta\xi)_w} \tag{10}$$

where

$$D_w = \left(\frac{\Gamma g^{\xi\xi} J \Delta\eta\Delta\zeta}{\Delta\xi}\right)_w \tag{11}$$

*2.2.2.1. For the diffusion resistance at the interface when solving the momentum equations and energy equation of the decoupled problem.* Considering that the region from the interface $w$ to node $P$ is a solid area, where the values of variable $\phi$ are the same for velocity and for temperature when the solid region is isothermal, the diffusion process actually only existed in the fluid area, i.e., only in the region from west node $W$ to face $w$; then,

$$\left(\Gamma \frac{\partial \phi}{\partial \xi}\right)_w = \Gamma_w \frac{\phi_w - \phi_W}{(\Delta\xi)_{Ww}} \tag{12}$$

Since in the transformed computational domain the grid is always uniform, $(\Delta\xi)_{Ww} = 0.5(\Delta\xi)_w$. In addition, $\phi_w = \phi_P = 0$ for momentum equations and $\phi_w = \phi_P = T_w$ for the energy equation of the decoupled problem; thus we yield,

$$\left(\Gamma \frac{\partial \phi}{\partial \xi}\right)_{\mathrm{w}} = \Gamma_{\mathrm{w}} \frac{\phi_{\mathrm{w}} - \phi_{\mathrm{W}}}{(\Delta\xi)_{\mathrm{Ww}}} = \Gamma_{\mathrm{w}} \frac{\phi_{\mathrm{w}} - \phi_{\mathrm{P}}}{0.5(\Delta\xi)_{\mathrm{w}}} \tag{13}$$

So for the fluid-solid decoupled problem, the diffusion flux through the interface $w$ is as follows.

$$J_{\mathrm{w}} = \Gamma_{\mathrm{w}} \left(\frac{g^{\xi\xi} J \Delta\eta\Delta\zeta}{0.5\Delta\xi}\right)_{\mathrm{w}} (\phi_{\mathrm{w}} - \phi_{\mathrm{P}}) \tag{14}$$

Thus, for the fluid-solid decoupled problem, the expression of diffusion conductance $D_w$ is as follows.

$$D_w = \frac{\Gamma_W}{\left(\frac{g^{\xi\xi} J \Delta\eta\Delta\zeta}{0.5\Delta\xi}\right)_w} \tag{15}$$

Moreover, the large coefficient method [17] is adopted to obtain the temperature of the solid area for the energy equation in the decoupled heat transfer problem.

*2.2.2.2. For the energy equation of the coupled heat transfer problem.* The temperature variables in staggered and collocated grid systems are both located at the main nodes. So, the treatment techniques for the energy equation in staggered grid systems can also be used in the collocated grid system. In reference [17], it is pointed out that when the harmonic-mean method is used to determine the effective diffusion coefficient for the interface to ensure the continuity of heat flux density through the interface at fluid and solid sides, in the nominal diffusion coefficient in Eq. (1), $\lambda/c_p$, the fluid specific heat should be used both for fluid and solid regions. In reference [14] this practice was adopted to solve the conjugated heat transfer problem between fin surface and fluid.

**2.2.3. Treatment of pressure and pressure correction equation at the fluid-solid interface.** Linear interpolation from the fluid side is adopted to calculate the pressure at the soild-fluid interface. In the pressure correction equation for the grid located in the fluid side near the interface, the coefficient of the pressure-correction equation related to the solid-fluid interface should be set to a very small value, say $10^{-25}$.

## 3. PHYSICAL AND MATHEMATICAL MODELS FOR SIMULATION OF A DIMPLED FIN-AND-TUBE SURFACE

### 3.1. Physical Models and Mathematical Formulation

The structures of the dimpled fin-and-tube surface and plain plate fin-and-tube surface are generally the same, except for the fin shape. To manufacture the dimpled fin, the reference plain plate fins are stamped in given locations, and then indentations and protrusions like the shape of the dimple are formed on two sides of the fin surface. A pictorial view of a plain plate fin-and-tube surface is shown in Figure 2 [47]. As can be seen there from the periodicity of the geometry, fluid flow and heat transfer can be regarded as periodic in both $y$- and $z$-directions. Hence, the region between the centerlines of two adjacent fins (A in Figure 2) or the region

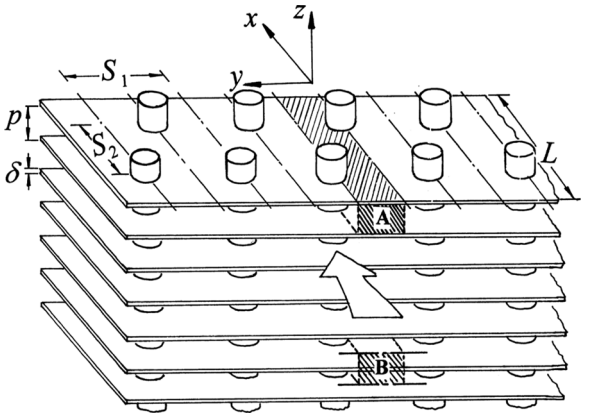


**Figure 2.** Pictorial view of plain fin-and-tube heat exchanger.

within which a fin surface is situated in its center (B in Figure 2) can be taken as the computational domain. Such a choice can be applied to both plain plate fin and other types of fin surfaces. Figure 3 shows the schematic diagram of the structure and geometrical parameter of a dimpled fin with two-row staggered tubes. In this fin surface, three-row staggered dimples are stamped, and the stamping directions of all dimples are the same. *RQA* and *RQB* represent the radius of the major and minor axes of the ellipse on the stamped surface, respectively, *HQD* represents dimple height, and *RA*, *RB*, and *RC* are the axes of the corresponding ellipsoid.

In the following investigation, practice B is adopted and the computational domain is extended in both the upstream and downstream parts with 1 time and 5 times of the computational fin length, respectively. The calculation parameters are shown in Table 1, and the fin collar outside diameter $d_o = D_0 + 2\delta$. The tube material is copper and the fin material is aluminum.

The general governing equation is expressed by Eq. (4). The mass, momentum, and energy equations can be written individually as follows.

Continuity equation

$$\frac{\partial}{\partial(\xi)}(\rho U) + \frac{\partial}{\partial\eta}(\rho V) + \frac{\partial}{\partial\zeta}(\rho W) = 0 \tag{16}$$

Momentum equations

$$\frac{\partial(\sqrt{g}\rho\phi V^i)}{\partial\xi^i} = \frac{\partial}{\partial\xi^i}\left(\Gamma_\phi g^{ii}\frac{\partial\phi}{\partial\xi^i}\sqrt{g}\right) - A_k^i\frac{\partial p}{\partial\xi^i} + \frac{\partial}{\partial\xi^i}\left(\Gamma_\phi g^{ji}\frac{\partial\phi}{\partial\xi^j}\sqrt{g}\right)(\phi = u, v, w) \tag{17}$$

Energy equations:

$$\frac{\partial(\sqrt{g}\rho\phi V^i)}{\partial\xi^i} = \frac{\partial}{\partial\xi^i}\left(\Gamma_\phi g^{ii}\frac{\partial\phi}{\partial\xi^i}\sqrt{g}\right) + \frac{\partial}{\partial\xi^i}\left(\Gamma_\phi g^{ji}\frac{\partial\phi}{\partial\xi^j}\sqrt{g}\right)(\phi = T) \tag{18}$$

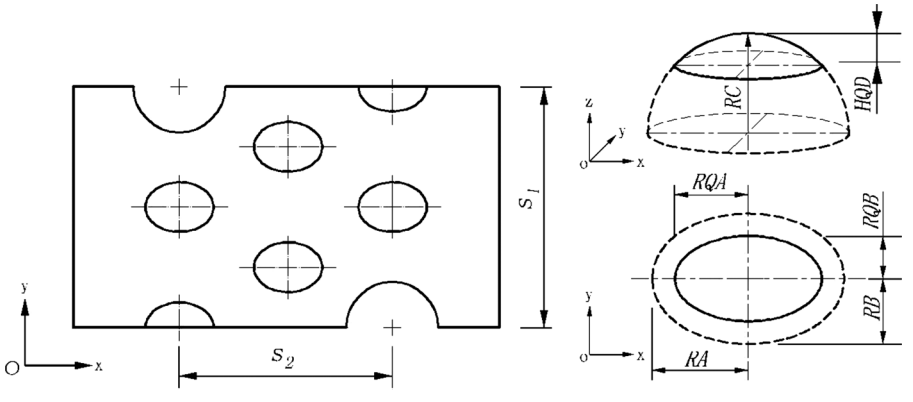


**Figure 3.** Schematic diagram of the structure and geometrical parameters of a dimpled fin.

**Table 1.** Geometric parameters of plain plate and dimple fins

| Fin type | Plain plate fin | Dimpled fin |
|---|---|---|
| Transverse tube spacing, $S_1$ | 25.0 mm | 50.0 mm |
| Longitudinal tube spacing, $S_2$ | 21.65 mm | 22 mm |
| Fin pitch, $F_P$ | 2.0 mm | 2.2 mm |
| Fin thickness, $\delta$ | 0.1 mm | 0.12 mm |
| Tube diameter, $D_o$ | 9.83 mm | 9.52 mm |
| Fin length, $l$ | 43.3 mm | 44.0 mm |

Because the governing equations are elliptic, boundary conditions are required for all boundaries of the computation domain. As indicated above, the fin surfaces are considered as part of the solution domain and no conditions are required at fin surfaces.

The boundary conditions in the physical domain are as follows.

At the inlet and outlet ($x$ coordinate).

At the inlet:

$$u = \text{const},\ T_{in} = \text{const},\ v = w = 0 \tag{19}$$

At the outlet

$$\frac{\partial u}{\partial x} = \frac{\partial v}{\partial x} = \frac{\partial w}{\partial x} = \frac{\partial T}{\partial x} = 0 \tag{20}$$

At the front and back sides ($y$ coordinate in Figure 3).

Fluid region

$$\frac{\partial u}{\partial y} = \frac{\partial w}{\partial y} = 0,\ v = 0,\ \frac{\partial T}{\partial y} = 0 \tag{21}$$

Fin surface region

$$u = v = w = 0 \tag{22}$$

Tube region

$$u = v = w = 0,\ T_w = \text{const} \tag{23}$$

Temperature condition for both fin and fluid regions

$$\frac{\partial T}{\partial y} = 0 \tag{24}$$

Boundary conditions at the upper and lower boundaries ($z$ coordinate). In the upstream extended region: symmetry condition, and in the fin coil region and the downstream extended region: periodic condition For the overall heat transfer process from the air side to fluid in the tube, the thermal resistance of the inner fluid side is much less than that of the air side. Additionally, the tube wall is made of copper,

which has very high thermal conductivity. Thus, the assumption of constant tube wall temperature is adopted here.

### 3.2. Grid Generation and Numerical Methods

A schematic diagram of the dimpled fin-and-tube surface is presented in Figure 3. The generation of the grid system for this complicated geometric structure is as follows. First, the grids in a projection surface of the dimpled structure are generated (as shown in Figure 4*a*), and then the projection plane are transformed into a curve surface based on the topological transformation relation. For the grid generation method of projection surface, the physical domain is divided into several subregions, and in different sub-region various grid generation methods can be chosen according to needs. In this article the initial grids were generated by one of the algebraic methods (two boundary method) [17], and the local grids were smoothed by the elliptic differential equation method. Figure 4*b* presents the three-dimensional grid of the fin part of the computational domain.

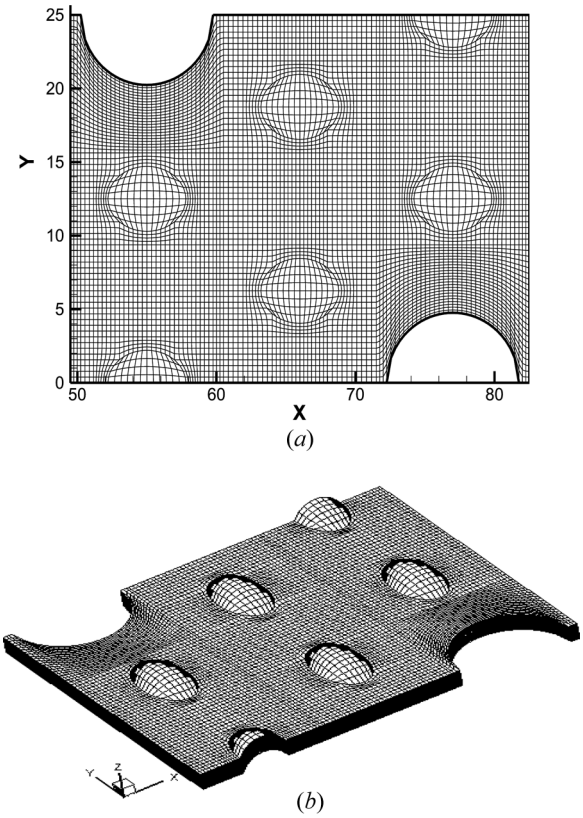


**Figure 4.** Grid systems of a dimpled fin (*a*) Grids of dimpled fin surface in projection surface (local); and (*b*) local three-dimensional grid of the fin part of the computational domain (not in scale).

The governing equations were discretized by the finite volume method. The power law is used to discretize both convective and diffusive terms in the momentum and energy equations; the SIMPLE algorithm for collocated-grids in body-fitted coordinate system is adopted. The elliptic equations are solved by the full-field computational method. As indicated above, the fin surfaces are considered as a part of the solution domain because of the conjugated nature of the problem. An array was introduced to distinguish the fluid and fin zones in the computational domain. In the iterative solution process for the algebraic equations of the 3-D problem, the ADI approach is adopted. In order to speed up the iteration convergence, variables in the coordinate with periodic boundary condition at its two ends, i.e., the $y$- and $z$-coordinates, are solved by the CTDMA method [48], and the TDMA method is adopted in the $x$-direction where the inlet and the outlet boundary conditions are non-periodic. The convergence criterion for the velocity is that the maximum mass residual of the cells is less than $2 \times 10^{-5}$.

A grid independence study is conducted, and the results are shown in Figure 5. From the variation trend it can be assumed that the grid system of $340 \times 68 \times 24$ can give a nearly grid-independent solutions. So, this grid system is adopted in numerical simulation.

### 3.3. Data Reduction Formula

From the numerical fields of velocity and temperature the relevant parameters are defined as follows.

The average heat transfer coefficient of the fin surface,

$$h_o = \Phi/(A_o \cdot \Delta T_m) \tag{25}$$

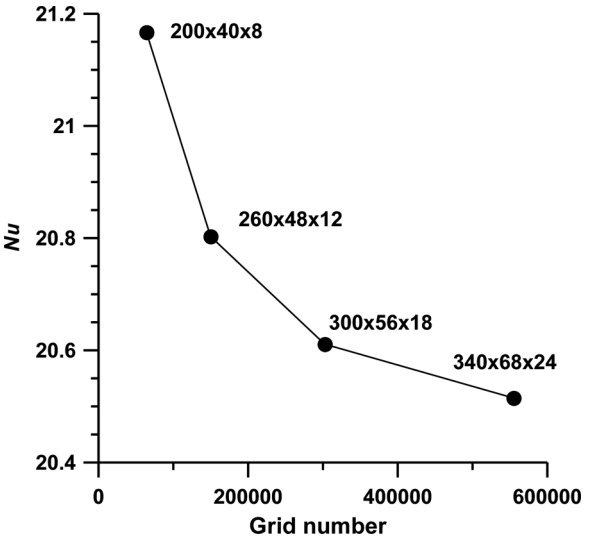


**Figure 5.** Variation of the predicted Nusselt number with grid numbers.

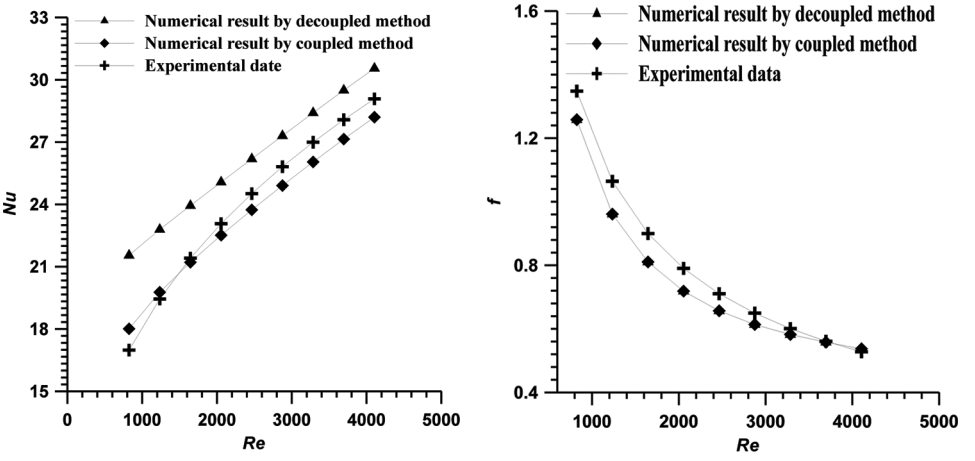


**Figure 6.** Comparison of Nu and $f$ between numerical results and experimental data. (*a*) Nusselt number comparison, and (*b*) friction factor comparison.

where $A_o$ includes the area of calculated tube outside surface (i.e., fin collar outside surface) between two adjacent fins and the area of the fin surface. For the fin part, the projection area is taken as the heat transfer area without considering the detail fin structures. It should be noted that taking the heat transfer area as the heat transfer coefficient defined in Eq. (25) actually includes the effect of the fin efficiency, which is quite convenient for the engineering application; $\Delta T_m$ is the logarithmic mean temperature difference between the hot and cold fluids and is defined as

$$\Delta T_m = \frac{\Delta T_{\max} - \Delta T_{\min}}{\ln \frac{\Delta T_{\max}}{\Delta T_{\min}}} \tag{26}$$

where

$$\Delta T_{\max} = \max(T_{in} - T_w, T_{out} - T_w), \Delta T_{\min} = \min(T_{in} - T_w, T_{out} - T_w) \tag{27}$$

Reynolds and Nusselt numbers

$$\mathrm{Re} = \frac{u_m \cdot d_o}{\nu_a}, \ \mathrm{Nu} = \frac{h_o d_o}{\lambda_a} \tag{28}$$

Darcy's friction coefficient

$$f = \frac{\Delta P}{l} \cdot d_o / (0.5 \cdot \rho \cdot u_m^2) \tag{29}$$

Mean synergy angle between velocity and temperature gradient

$$\theta_m = \arccos \frac{\sum \vec{V} \cdot \nabla T dV}{\sum \left|\vec{V}\right| \cdot |\nabla T| dV} \tag{30}$$

### 3.4. Code Validation

In order to check the reliability of the developed code, a numerical simulation is first conducted for the airside of the plain plate fin-and-tube heat transfer surface with two-row staggered tubes, and the results are compared with that of the experimental results. The structure parameter shown in Table 1 are adopted from reference [49].

Numerical treatments for the extension of the domain, the boundary conditions and the conjugated solution scheme are very similar to the dimpled surface presented above; hence, it will not be restated here. A grid system of $320 \times 58 \times 20$ grids is adopted in numerical simulation. The convergence criterion for the velocity is that the maximum mass residual of the cells is less than $2 \times 10^{-5}$. The heat transfer rate in the airside can be obtained by two calculation methods: the first is through mean enthalpy difference between inlet and outlet: $\Phi_h = q_m c_p (T_{out} - T_{in})$. The second is through Fourier's law at the fin surface: $\Phi_c = \sum -\lambda \nabla T \cdot \Delta \vec{A}$ The convergence criterion for the temperature is that the relative difference of the two heat transfer rates should be less than a specified small value; 1% is adopted in this study.

The numerical results are compared with the experimental data in reference [49]. The temperatures of the fin are considered in two ways: in one way the temperature of the fin sheet is the same as that of the tube wall; in the other, the temperature of the fin sheet is solved simultaneously. For the simplicity of presentation, the two ways are called decoupled and coupled methods, respectively. The results show that the Nusslet number of the decoupled method is higher than the latter, as can be seen in Figure 6. The Nusselt number by the conjugated computation is closer to the experimental data compared with the decoupled results with the maximum deviation of the Nusselt number being 17.2% and 6.04%, respectively. Figure 7 shows the comparison of the friction coefficient $f$ between the two numerical results and experimental data. Since constant thermophysical properties are assumed, the friction factor predicted by the coupled and decoupled methods are the same as can be seen

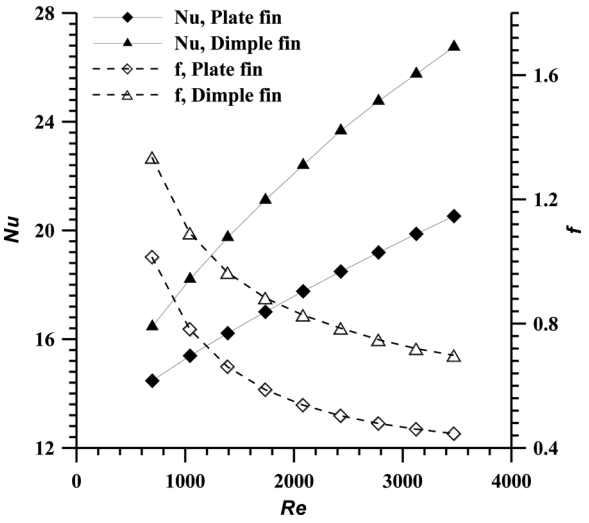


**Figure 7.** Comparison of Nu and $f$ between reference plain plate fin and dimpled fin.

from the figure, with the maximum deviation being 9.95% between numerical results and the experimental data.

In order to reveal the effects of the decoupled and coupled methods on heat transfer characteristics of the fin surface at different inlet velocities, the fin efficiency $\eta$ was introduced. The parameter $\eta$ presents the ratio of the actual heat transfer rate obtained by the coupled method to the heat transfer rate assuming the temperature of fin surface is equal to the tube wall temperature $T_w$, which can be obtained by the decoupled method. Figure 8 presents the fin efficiency under different Reynolds number. It can be seen that the efficiency of the plain plate fin ranges from about 0.8 at higher inlet velocity (around 5 m/s) to 0.92 at lower inlet velocity (around 1.0 m/s). The results show that the influence of fin efficiency is needed to be considered. Thus, the coupled method is used in the following numerical simulations.



## 4. RESULTS AND DISCUSSION

### 4.1. Comparison of Flow and Heat Transfer Characteristics between Plain Plate Fin and Basic Dimpled Fins

In this case, dimple imprint major and minor axes of basic fins have the same length and are equal to the dimple imprint radius, i.e., $RQA = RQB = RQ_b$. Nondimensionalize structure parameters of dimple by the dimple imprint radius $RQ_b$ are shown in Table 2 (basic fins). The inlet velocity of air is 1.0 m/s–5.0 m/s.

Figure 7 presents the comparison of the average Nusselt number and friction factor between a reference plain plate fin and basic dimpled fin with the same conditions. It can be seen from the figure that the dimpled fin surface presents a higher Nusselt number and friction factor than those of the reference plain plate fin. The thermal performance of the two types of fin surfaces are evaluated on the log-log-based performance comparison figure proposed in reference [50]. Figure 9 presents the comparison figure. In region 1, heat transfer is actually deteriorated based on identical pumping power. In region 2, heat transfer is enhanced based on identical pumping power but deteriorated based on identical pressure drop. In region 3, heat transfer is enhanced based on identical pressure drop but the increase in friction factor is larger than the enhancement of heat transfer at identical flow rate. In region 4, heat transfer enhancement ratio is larger than friction factor increase ratio based on identical flow rate. It can be found that this enhancing technique is in the third region, a favorite region for heat transfer enhancement, where the heat transfer is

**Table 2.** Nondimensional dimple parameters by basic imprint radius of dimple

| | Nondimensional parameters | | | | | |
|---|---|---|---|---|---|---|
| Name | *RQA* | *RQB* | *HQD* | *RA* | *RB* | *RC* |
| Basic fin | 1 | 1 | 0.66 | 1.143 | 1.143 | 1.314 |
| Fin VH1 | 1 | 1 | 0.286–0.743 | 1.606–1.110 | 1.606–1.110 | 1.314 |
| Fin VH2 | 0.718–1.038 | 0.718–1.038 | 0.286–0.743 | 1.153 | 1.153 | 1 |
| Fin VRA | 0.5–1.464 | 1.14 | 0.66 | 0.576–1.688 | 1.314 | 1.314 |
| Fin VRB | 1.14 | 0.714–1.464 | 0.66 | 1.314 | 0.824–1.688 | 1.314 |

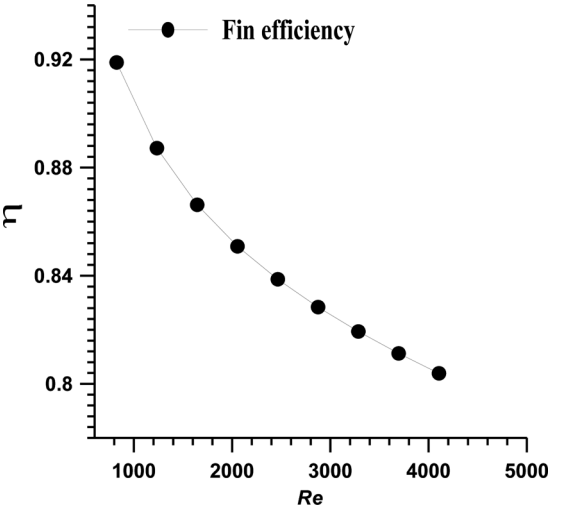


**Figure 8.** Fin efficiency under different Reynolds numbers.

enhanced under identical pressure drop and identical pumping power. Moreover, in the figure, nine working points are presented whose corresponding velocity of plain plate fin is 1.0, 1.5, 2.0, 2.5, 3.0, 3.5, 4.0, 4.5, and 5.0 m/s, from left to right, respectively. According to reference [50], the heat transfer enhancement ratio $Q_d/Q_0$ is determined as follows.

$$\frac{Q_d}{Q_0} = \left(\frac{\mathrm{Nu}_d}{\mathrm{Nu}_0}\right) \Big/ \left(\frac{f_d}{f_0}\right)^{\frac{m2}{a+m1}} \tag{31}$$

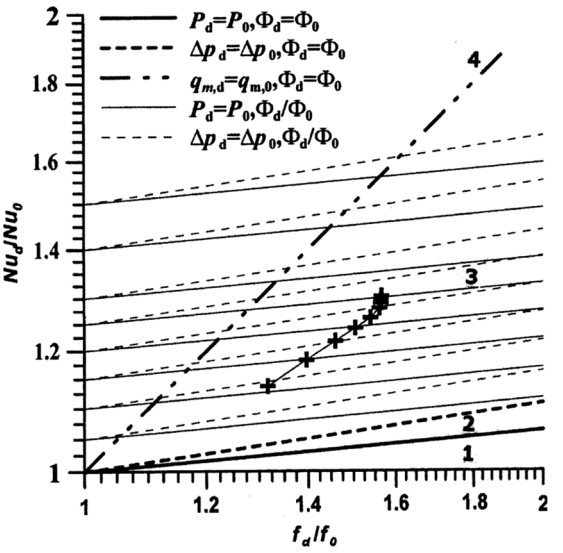


**Figure 9.** Performance comparisons between the reference and dimpled fin-and-tube surfaces.

where $m1$ and $m2$ are the exponent in $f_d = C_1 \mathrm{Re}^{m1}$, $\mathrm{Nu}_d = C_2 \mathrm{Re}^{m2}$of the reference, structure, $a = 2$ for identical pressure constraint, and $a = 3$ for the identical pumping power constraint. For the details of derivation, reference [50, 51] may be consulted. The specific values of $m1$ and $m3$ for the plain plate fin adopted are $m1 = -0.509$ and $m2 = 0.219$, respectively, which are obtained from data reduction of the numerical results.

Within the inlet velocity range studied, the obtained heat transfer enhancement ratio of the dimpled fin over the reference plain plate fin are 11.0%–25.3% and 9.2%–22.0% for the identical pumping power constraint and identical pressure drop constraint, respectively (see Table 3).

The relative higher heat transfer enhancement of the dimpled fin surface can be attributed to the following two facts. First, longitudinal vortices are generated by the dimpled indentations, which enhances the local heat transfer downstream with not too much pressure drop. Second, when fluid flow through the protrusions or turbulators, some horseshoe vortices are formed in the first half of the protrusions; thus, the local heat transfer increases as the horseshoe vortices develops, and some transverse vortices can be formed in the tail of protrusion, which increases the friction drag slightly.

Figure 10 shows the comparison of the mean synergy angle between the reference plain plate fin and dimpled fin at different Reynolds numbers. The synergy angle of the dimpled fin surface is lower than that of the reference fin surface at the same Reynolds number. This implies that the vortices introduced by the existence of dimples improve the synergy between velocity and the temperature gradient.

### 4.3. Influence of Dimple Height on Flow and Heat Transfer Performance

As indicated at the beginning of this section, a dimple has six geometric parameters: *RA, RB, RC, RQA, RQB*, and *HQD*. The collection of the specific values adopted in the above prediction will be called the basic case. The effect of the dimple height is first studied. Dimple height can be changed by different ways: by either changing some lengths of the ellipsoid axes *RA* and *RB*, or changing the lengths of the axes of the ellipse in stamped surface. In order to compare the performance

**Table 3.** The Performance comparison between dimpled fin and plain plate fin surfaces

| Identical pumping power ($P_d = P_0$) | | Identical pressure drop ($\Delta p_d = \Delta p_0$) | |
|---|---|---|---|
| Velocity of plate fin m/s | $(Q_d - Q_0)/Q_0$ % | Velocity of plate fin m/s | $(Q_d - Q_0)/Q_0$ % |
| 1.0 | 11.0 | 1.0 | 9.2 |
| 1.5 | 14.9 | 1.5 | 12.7 |
| 2.0 | 17.8 | 2.0 | 15.2 |
| 2.5 | 19.8 | 2.5 | 17.0 |
| 3.0 | 21.4 | 3.0 | 18.4 |
| 3.5 | 23.1 | 3.5 | 19.9 |
| 4.0 | 24.1 | 4.0 | 20.8 |
| 4.5 | 24.6 | 4.5 | 21.4 |
| 5.0 | 25.3 | 5.0 | 22.0 |

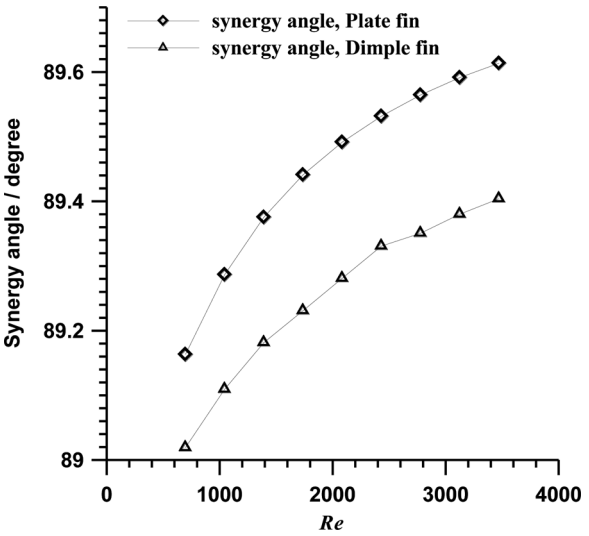


**Figure 10.** Comparison of synergy angle between reference plate and dimpled fins.

of dimpled fins with different dimple height, the following two cases are studied at inlet velocity of 2 m/s: one maintains *RQA*, *RQB*, and *RC* the same as the basic case and the dimpled high *HQD* vary with the values of *RA* and *RB* (Fin VH1); the other maintains *RA*, *RB*, and *RC* the same as the basic case and the values of *RQA* and *RQB* are changed (Fin VH2). The dimple geometric parameters of fins VH1 and VH2 are shown in Table 2.

Figure 11 shows the comparison of the Nusselt number and friction factor of dimpled fin surfaces with different dimple heights. It can be found from the figure

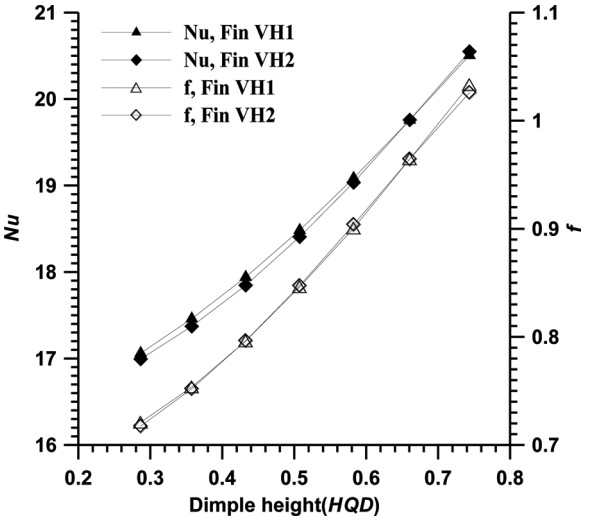


**Figure 11.** Nu and *f* of dimple fin surfaces with different dimpled heights.

that results of the two cases are very close. This indicates that the way of changing the dimple height does not have an appreciable effect. The increase of the Nusselt number and friction factor with the dimple height are resulted from the enhancement of the fluid disturbance augmented by the increased dimple height.

### 4.4. Influences of Ellipse Major and Minor Axes on the Performance of Dimpled Fin Surface

In order to investigate the influence of the major and minor axes of ellipse in stamped surface on the flow and heat transfer of a dimpled fin surface, the following two cases are studied at 2 m/s inlet velocity: one maintains *RC, RB* the same as the reference case, and the value of *RA* changes as the change of the major axes of ellipse on a stamped surface *RQA* (Fin VRA); the latter maintains *RC, RA* the same as the reference case, and the value of *RB* change as the change of the minor axes of ellipse *RQB* (Fin VRB). The corresponding parameters of dimple are shown in Table 2.

Figure 12 shows the Nusselt number and friction factor of dimpled fin surfaces with different major and minor axes of ellipse in stamped surface. It can be seen from Figure 12 that the Nusselt number and friction factor reduce as the increase of the major axes *RQA* of ellipse and increases as the minor axes *RQB* increases. It is also found that the mean synergy angle increases with the increase of the major axes of ellipse. That is because the protrusion shape is aligned along the major axes in the streamline direction, and the increase of the major axes leads to the decrease of fluid disturbance generated by the protrusion; hence, both the Nusselt number and friction factor reduces and the synergy between velocity and temperature becomes worse. At the same time, the results are just the opposite when the minor axes of ellipse on the stamped surface increases.

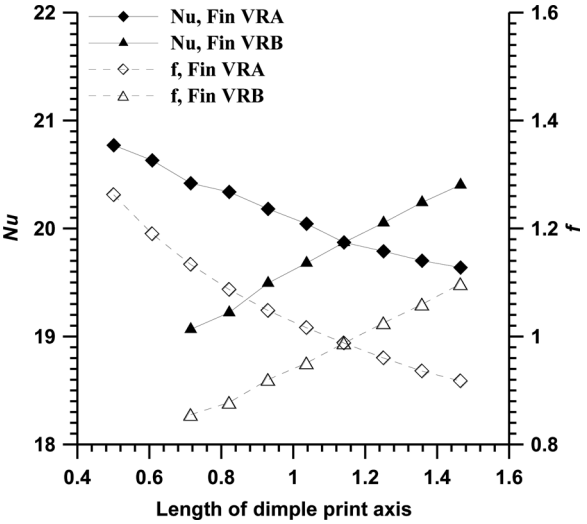


**Figure 12.** Nu and *f* of dimple fin surfaces with different lengths of dimpled print major or minor axes.

Finally, it is interesting to note the flow regimes: laminar or turbulent. The Re numbers based on the tube diameter (Eq. (28)) range from 800 to 4200 and 600 to 3600 for the plain plate and dimpled fins, respectively. The laminar model is used in our simulation. Following are our basic considerations.

First, we take the flow in the fin-and-tube configuration as the flow across a tube bank. Then according to the well-known correlation from Zhukauskas [52] when the Reynolds number based on the tube diameter is less than $2 \times 10^5$, the exponent in the Reynolds number is 0.6, while for $\mathrm{Re} = 2 \times 10^5$ the exponent is 0.8. From the authors' understanding, $\mathrm{Re} = 2 \times 10^5$ may be regarded as the criterion of fully turbulent flow of tube banks. Second, if we consider such a flow as the flow in a rectangular duct, then the Reynolds number based on the equivalent diameter equals 2300 may be regarded as the upper limit of laminar flow. In our study, the Reynolds number based on the tube diameter is far less than $2 \times 10^5$, and its maximum value based on the equivalent diameter is 1814, which is less than 2300. Thus, we take the flow as laminar.



## 5. CONCLUSION

In this article, in order to numerically simulate the fluid flow and heat transfer performance of the dimpled fin-and-tube structure a code based on the nonorthogonal curvilinear coordinates is developed with a collocated grid system generated by the two-boundary method. The code is first validated by the simulation of a plain plate fin-and-tube structure for which reliable test data are available. The heat transfer between fin and fluid simulated by coupled and decoupled methods are compared. After the validation, performance predictions for the dimpled and reference plain plate fin-and-tube surfaces are conducted in a wide variation range of the inlet velocity (from 1.0 m/s to 5.0 m/s). The major conclusions are as follows.

- For the plate fin-and-tube type complicated structures, the heat transfer of the fin surface should be simulated by the coupled method, i.e, both the fin and the fluid temperature should be solved simultaneously.
- Compared with the reference plain plate fin-and-tube structure, heat transfer rates of the basic dimpled fin surface increase by 13.8%–30.3%, and friction factors increase by 31.6%–56.5% for the identical flow rate constraint; And for the identical pumping power constraint and identical pressure drop constraint the heat transfer rates of dimpled fin are increased by 11.0%–25.3% and 9.2%–22.0%, respectively.
- For the dimpled fin-and-tube structure the Nusselt number and friction factor increase with the increase in the dimple height or the minor axes of ellipse in stamped surface; and both of them decrease with the increase of major axes of ellipse in stamped surface.
- The existence of dimples in the fin surface improves the synergy between fluid velocity and temperature gradient.

## REFERENCES

1. Z. Y. Guo, D. Y. Li, and B. X. Wang, A Novel Concept for Convective Heat Transfer Enhancement, *Int. J. Heat Mass Transfer*, vol. 41, pp. 2221–2225, 1998.

2. W. Q. Tao, Z. Y. Guo, and B. X. Wang, Field Synergy Principle for Enhancing Convective Heat Transfer—Its Extension and Numerical Verifications, *Int. J. Heat Mass Transfer*, vol. 45, no. 18, pp. 3849–3856, 2002.
3. W. Q. Tao, Y. L. He, Q. W. Wang, Z. G. Qu, and F. Q. Song, A Unified Analysis on Enhancing Single Phase Convective Heat Transfer with Field Synergy Principle, *Int. J. Heat Mass Transfer*, vol. 45, no. 24, pp. 4871–4879, 2002.
4. Z. Y. Guo, W. Q. Tao, and R. K. Shah, The Filed Synergy (Coordination) Principle and its Applications in Enhancing Single Phase Convective Heat Transfer, *Int. J. Heat Mass Transfer*, vol. 48, pp. 1797–1807, 2005.
5. Y. P. Cheng, Z. G. Qu, W. Q. Tao, and Y. L. He, Numerical Design of Efficient Slotted Fin Surface Based on the Field Synergy Principle, *Numer. Heat Transfer*, vol. 45, pp. 517–538, 2004.
6. W. Q. Tao, Y. L. He, Z. G. Qu, and Y. P. Cheng, Applications of the Field Synergy Principle in Developing New Type Heat Transfer Enhanced Surfaces, *J. of Enhanced Heat Transfer*, vol. 11, no. 4, pp. 433–449, 2004.
7. Y. L. He, W. Q. Tao, F. Q. Song, and W. Zhang, Three-Dimensional Numerical Study of Heat Transfer Characteristics of Plain Plate Fin-and-Tube Heat Exchangers from Viewpoint of Field Synergy Principle, *Int. J. Heat Fluid Flow*, vol. 26, pp. 459–473, 2005.
8. E. M. Sparrow and W. Q. Tao, Enhanced Heat Transfer in a Flat Rectangular Duct with Streamwise Periodic Disturbances at One Principle Wall, *ASME J. Heat Transfer*, vol. 105, pp. 851–861, 1983.
9. E. M. Sparrow and W. Q. Tao, Symmertic vs. Asymmetric Periodic Structures at Walls of a Heated Flow Passage, *Int. J. Heat Mass Transfer*, vol. 27, pp. 2133–2144, 1984.
10. H. Z. Huang and W. Q. Tao, An Experimental Study on Heat/Mass Transfer and Pressure Drop Characteristics for Arrays of Non-Uniform Plate Length Positioned Obliquely to the Flow Direction, *ASME J. Heat Transfer*, vol. 115, pp. 568–575, 1993.
11. S. S. Lue, H. Z. Huang, and W. Q. Tao, Experimental Study on Heat Transfer and Pressure Drop Characteristics in the Developing Region for Arrays of Obliquely Positioned Plates of Nonuniform Length, *Exper. Therm. and Fluid Sci.*, vol. 7, no. 1, pp. 30–38, 1993.
12. B. Yu, J. H. Nie, Q. W. Wang, and W. Q. Tao, Experimental Study on the Pressure Drop and Heat Transfer Characteristics of Tubes with Internal Wave-Like Longitudinal Fins, *Heat and Mass Transfer*, vol. 35, no. 1, pp. 65–73, 1999.
13. Z. X. Yuan, W. Q. Tao, and X. T. Yan, Experimental Study on Heat Transfer in Ducts with Winglet Disturbances, *Heat Transfer Eng.*, vol. 24, no. 2, pp. 76–84, 2003.
14. Z. G. Qu, W. Q. Tao, and Y. L. He, Three Dimensional Numerical Simulation on Laminar Heat Transfer and Fluid Flow Characteristics of Strip Fin Surface with X-Arrangement of Strips, *ASME J. Heat Transfer*, vol. 126, pp. 697–707, 2004.
15. Y. B. Tao, Y. L. He, Z. G. Wu, and W. Q. Tao, Three-Dimensional Numerical Study and Field Synergy Principle Analysis of Wavy Fin Heat Exchangers with Elliptic Tubes, *Int. J. Heat and Fluid Flow*, vol. 28, pp. 1531–1544, 2007.
16. S. V. Patankar, *Numerical Heat Transfer and Fluid Flow*, McGraw-Hill, New York, 1980.
17. W. Q. Tao, *Numerical Heat Transfer*, 2nd ed., Xi'an Jiaotong University Press, Xi'an, P.R. China, 2001.
18. C. M. Rhie and W. L. Chow, A Numerical Study of the Turbulent Flow Past an Isolated Airfoil with Trailing Edge Separations, *AIAA J.*, vol. 21, pp. 1525–1552, 1983.
19. M. Peric, R. Kessler, and G. Scheuerer, Comparison of Finite Volume Numerical Methods with Staggered and Collocated Grids, *Compt. Fluids*, vol. 16, pp. 389–403, 1988.
20. B. Yu, W. Q. Tao, J. J. Wei, Y. Kawaguchi, T. Tagawa, and H. Ozoe, Discussion on Momentum Interpolation Method for Collocated Grids of Incompressible Flow, *Numer. Heat Transfer B*, vol. 42, pp. 141–166, 2002.

21. Z. G. Qu, W. Q. Tao, and Y.L. He, Implementation of CLEAR Algorithm on Collocated Grid System and Application Examples, *Numer. Heat Transfer B*, vol. 46, pp. 65–96, 2005.
22. D. L. Sun, Z. G. Qu, Y. L. He, and W. Q. Tao, Implementation of an Efficient Segregated Algorithm—IDEAL on 3-D Collocated Grid System, *Chinese Sci. Bull.*, vol. 54, pp. 929–942, 2009.
23. S. V. Patankar, A Numerical Method for Conduction in Composite Materials, Flow in Irregular Geometries and Conjugate Heat Transfer, In *Proc. of the Sixth Int. Heat Transfer Conf.*, vol. 3, pp. 297–302, 1978.
24. B. W. Webb and S. Ramadhyani, Conjugate Heat Transfer in a Channel with Staggered Ribs, *Int. J. Heat Mass Transfer*, vol. 29, pp. 1679–1687, 1986.
25. W. Q. Tao, Conjugated Laminar Convective Heat Transfer from Internally Finned Tubes, *ASME J. Heat Transfer*, vol. 109, pp. 791–795, 1987.
26. W. Shyy and J. Burke, Study on Iterative Characteristics of Convective Diffusive and Conjugate Heat Transfer Problems, *Numer. Heat Transfer B*, vol. 25, pp. 163–176, 1994.
27. C. Y. Zhao and W. Q. Tao, Natural Convections in Conjugated Single and Double Enclosure, *Heat Mass Transfer*, vol. 30, pp. 175–182, 1995.
28. N. K. Anand, C. D. Chin, and J. G. McMath, Heat Transfer in Rectangular Channels with a Series of Normally In-Line Positioned Plates, *Numer. Heat Transfer A*, vol. 27, pp. 19–34, 1995.
29. M. Fiebig, Embedded Vortices in Internal Flow: Heat Transfer and Pressure Loss Enhancement, *Int. J. of Heat and Fluid Flow*, vol. 16, no. 5, pp. 376–388, 1995.
30. J. M. Wu and W. Q. Tao, Investigation on Laminar Convection Heat Transfer in Fin-and-Tube Heat Exchangers in Aligned Arrangement with Longitudinal Vortex Generator from Viewpoint of Field Synergy Principle, *Appl. Therm. Eng.*, vol. 27, pp. 2609–2617, 2007.
31. L. T. Tian, Y. L. He, Y. G. Lei, and W. Q. Tao, Numerical Study of Fluid Flow and Heat Transfer in a Flat Plate Channel with Longitudinal Vortex Generators by Applying Field Synergy Principle Analysis, *Int. Comm. Heat Mass Transfer*, vol. 36, pp. 111–120, 2009.
32. R. Y. Myose and R. F. Blackwelder, Controlling the Spacing of Streamwise Vortices on Concave Walls, *AIAA J.*, vol. 29, no. 11, pp. 1901–1905, 1991.
33. T. Kimura and M. Tsutahara, Fluid Dynamic Effects of Grooves on Circular Cylinder Surface, *AIAA J.*, vol. 29, no. 12, pp. 2062–2068, 1991.
34. V. N. Afanasyev, Y. P. Chudnovsky, A. I. Leontiev, and P. S. Roganov, Turbulent Flow Friction and Heat Transfer Characteristics for Spherical Cavities, *Exper. Therm. and Fluid Sci.*, vol. 7, pp. 1–8, 1993.
35. V. S. Kesarev and A. P. Kozlov, Convective Heat Transfer in Turbulized Flow Past a Hemispherical Cavity, *Heat Transfer Res.*, vol. 25, no. 2, pp. 156–160, 1993.
36. M. Ya. Belen'kiy, M. A. Gotovskiy, B. M. Lekakh, B. S. Forkin, and K. S. Dolgushin, Heat Transfer Augmentation Using Surfaces Formed by a System of Spherical Cavities, *Heat Transfer Res.*, vol. 25, no. 2, pp. 196–203, 1993.
37. J. Chin, H. Muller-steinHagen, and G. G. Duffy, Heat Transfer Enhancement in Dimpled Tubes, *Appl. Therm. Eng.*, vol. 21, pp. 535–547, 2001.
38. G. I. Mahmood, M. L. Hill, D. L. Nelson, P. M. Ligrani, H. K. Moon, and B. Glezer, Local Heat Transfer above a Dimpled Surface in a Channel, *J. of Turbomachinery*, vol. 123, pp. 115–123, 2001.
39. N. Syred, A. Khalatov, A. Kozlov, A. Shchukin, and R. Agachev, Effect of Surface Curvature on Heat Transfer and Hydrodynamics within a Single Hemispherical Dimple, *J. of Turbomachinery*, vol. 123, pp. 609–613, 2001.
40. P. M. Ligrani, G. I. Mahmmod, J. L. Harrison, C. M. Clayton, and D. L. Nelson, Flow Structure and Local Nusselt Number Variations in a Channel with Dimples and Protrusions on Opposite Walls, *Int. J. of Heat and Mass Transfer*, vol. 44, pp. 4413–4425, 2001.

41. P. M. Ligrani, J. L. Harrison, G. I. Mahmmod, and M. L. Hill, Flow Structure due to Dimple Depressions on a Channel Surface, *Physics of Fluids*, vol. 13, no. 11, pp. 3442–3451, 2001.
42. G. I. Mahmood and P. M. Ligrani, Heat Transfer in a Dimpled Channel: Combined Influences of Aspect Ratio, Temperature Ratio, Reynolds Number, and Flow Structure, *Int. J. of Heat and Mass Transfer*, vol. 45, pp. 2011–2020, 2002.
43. P. M. Ligrani, M. M. Oliveria, and T. Blaskovich, Comparison of Heat Transfer Augmentation Techniques, *AIAA J.*, vol. 41, no. 3, pp. 337–362, 2003.
44. H. Wee, Q. Zhang, P. M. Ligrani, and S. Narasimhan, Numerical Predictions of Heat Transfer and Flow Characteristics of Sinks with Ribbed and Dimpled Surfaces in Laminar Flow, *Numer. Heat Transfer A*, vol. 53, pp. 1156–1175, 2008.
45. W. Shyy, Element of Pressure-Based Computational Algorithms for Complex Fluid Flow and Heat Transfer, in J. P. Hartnett and T. F. Irvine (ed.), *Advances in Heat Transfer*, vol. 24, Academic Press, San Diego, pp. 191–275, 1994.
46. J. S. Wang. *Tensor Analysis with Applications*, Higher Education Press, Beijing, 1987.
47. W. Q. Tao, Y. P. Cheng, and T. S. Lee, The Influence of Strip Location on the Pressure Drop and Heat Transfer Performance of a Slotted Fin, *Numer. Heat Transfer, A*, vol. 52, pp. 463–480, 2007.
48. K. M. Kelkar, D. Choudhury, and W. J. Minkowycz, Numerical Method for the Computation of Flow in Irregular Domains that Exhibit Geometric Periodicity using Nonstaggered Grids, *Numer. Heat Transfer B*, vol. 31, pp. 1–21, 1997.
49. H. J. Kang, W. Li, H. Z. Li, R. C. Xin, and W. Q. Tao, Experimental Study on Heat Transfer and Pressure Drop for Plane Fin-and-Tube Heat Transfer Exchanger, *J. of Xi'an Jiaotong University*, vol. 1, pp. 91–98, 1994.
50. J. F. Fan, W. K. Ding, J. F. Zhang, Y. L. He, and W. Q. Tao, A Performance Evaluation Plot of Enhanced Heat Transfer Techniques Oriented for Energy-Saving, *Int. J. of Heat Mass Transfer*, vol. 52, pp. 33–44, 2009.
51. J. F. Fan, Studies on Air Heat Transfer Enhancement Techniques and Performance Evaluation Plots for Enhancing Techniques, Dissertation of Xi'an Jiaotong University, P.R. China, 2010.
52. A. A. Zhukauskas, *Convective Heat Transfer in Heat Exchangers*, Science Press, Moskva, 1982.